Microchimica Acta (2021) 188: 182
https://doi.org/10.1007/s00604-021-04838-6

ORIGINAL PAPER

Electrochemical immunosensor development based on core-shell high-crystalline graphitic carbon nitride@carbon dots and $Cd_{0.5}Zn_{0.5}S$/d-$Ti_3C_2T_x$ MXene composite for heart-type fatty acid–binding protein detection

Ceren Karaman[1] · Onur Karaman[2] · Necip Atar[3] · Mehmet Lütfi Yola[4]

Received: 23 March 2021 / Accepted: 26 April 2021 / Published online: 7 May 2021

Abstract

Acute myocardial infarction (AMI) is a significant health problem owing to its high mortality rate. Heart-type fatty acid–binding protein (h-FABP) is an important biomarker in the diagnosis of AMI. In this work, an electrochemical h-FABP immunosensor was developed based on $Cd_{0.5}Zn_{0.5}S$/d-$Ti_3C_2T_x$ MXene (MXene: Transition metal carbide or nitride) composite as signal amplificator and core-shell high-crystalline graphitic carbon nitride@carbon dots (hc-g-C_3N_4@CDs) as electrochemical sensor platform. Firstly, a facile calcination technique was applied to the preparation of hc-g-C_3N_4@CDs and immobilization of primary antibody was performed on hc-g-C_3N_4@CDs surface. Then, the conjugation of the second antibody to $Cd_{0.5}Zn_{0.5}S$/d-$Ti_3C_2T_x$ MXene was carried out by strong π-π and electrostatic interactions. The prepared electrochemical h-FABP immunosensor was characterized by transmission electron microscopy (TEM), scanning electron microscopy (SEM), x-ray diffraction (XRD) method, Fourier-transform infrared spectroscopy (FTIR), x-ray photoelectron spectroscopy (XPS), cyclic voltammetry (CV), and electrochemical impedance spectroscopy (EIS). The prepared electrochemical h-FABP immunosensor indicated a good sensitivity with detection limit (LOD) of 3.30 fg mL^{-1} in the potential range +0.1 to +0.5 V. Lastly, low-cost, satisfactory stable, and environmentally friendly immunosensor was presented for the diagnosis of acute myocardial infarction.

Keywords h-FABP protein · hc-g-C_3N_4@CDs · $Cd_{0.5}Zn_{0.5}S$/d-$Ti_3C_2T_x$ MXene · Immunosensor · Voltammetry

Introduction

Myocardial infarction is the insufficient blood supply of the heart muscle due to the blockage of the coronary arteries that feed the heart. Acute myocardial infarction (AMI) is an important public health problem due to the fact that it is a disease that can result in death and is generally seen in all age groups and serious complications occur afterwards [1, 2]. h-FABP as AMI biomarker has an important function in the therapy of AMI [3]. When the myocardium was damaged, the release of h-FABP into circulation during 90 min occurred, suggesting that h-FABP detection could be easily performed in a plasma sample. This situation is correlated with the prognosis of AMI [4]. Up to now, several methods such as enzyme-linked immunosorbent assay (ELISA) [5] and fluorescence [6] were developed for h-FABP detections. Nonetheless, these techniques are not convenient because of the cost, the consumption of many chemicals, and the time-consuming sample preparation procedures. Thus, the development of sensitive, convenient, and fast analytical techniques for h-FABP detection is significant in terms of the preliminary diagnosis of AMI. Especially, sensitive and simple electrochemical techniques used in place of traditional techniques have attracted interest due to efficient operation and less chemical usage [7–9].

Immunosensors are biosensors that use antibodies as recognition elements. It is based on interactions between an

✉ Mehmet Lütfi Yola
mlutfi.yola@hku.edu.tr

[1] Vocational School of Technical Sciences, Department of Electricity and Energy, Akdeniz University, Antalya, Turkey

[2] Vocational School of Health Services, Department of Medical Imaging Techniques, Akdeniz University, Antalya, Turkey

[3] Faculty of Engineering, Department of Chemical Engineering, Pamukkale University, Denizli, Turkey

[4] Faculty of Health Sciences, Department of Nutrition and Dietetics, Hasan Kalyoncu University, Gaziantep, Turkey

antibody and an antigen on the surface of a transducer. The main basis of all immunosensors is the specificity of molecular recognition of antigens to form a stable complex. With the strong binding between these biomolecules, immunosensors show high selectivity and very high sensitivity, making them attractive for many applications in different fields of science [10]. Especially, the replacement of simple electrochemical techniques with conventional methods has gained substantial attention due to the efficient operation feature and less chemical consumption [7–9, 11–18]. For example, an amperometric immunosensor for h-FABP detection was presented based on screen-printed carbon electrode and this amperometric immunosensor showed a linearity range from 4.0 to 250.0 ng mL^{-1} with a LOD of 4.0 ng mL^{-1} [19]. In addition, impedimetric immunosensor was prepared based on gold electrode modified with 11-mercaptoundecanoic acid, suggesting linearity of 98.0 pg mL^{-1}–100.0 ng mL^{-1} with a LOD of 117.0 pg mL^{-1} for h-FABP recognition [20]. Capacitive immunosensor based on gold electrode modified with 11-mercaptoundecanoic acid was also constructed and showed a LOD of 0.84 ng mL^{-1} for h-FABP recognition [21]. Finally, electrochemiluminescence immunosensor for h-FABP recognition based on 2D-nickel metal-organic framework nanosheets was developed and a LOD of 44.5 fg mL^{-1} was obtained [22].

Because g-C_3N_4 with band gap of 2.7 eV has interesting chemical properties and high stability, it has been seen as a promising catalyst in recent years [23]. Nonetheless, owing to its specific surface area and the recombination of electron-hole pairs, the sensor/catalysis performance is generally limited [24]. To improve the sensor/catalysis performances, several techniques have been developed such as element doping [25], morphological control [26], and coupling treatment [27]. In addition, some studies demonstrated g-C_3N_4's low crystallinity properties owing to unreacted –NH_2 groups [28]. These –NH_2 groups have been considered as structural defects which result in low sensor/catalysis activity [29]. Hence, hc-g-C_3N_4 has attracted attention in comparison with g-C_3N_4 owing to high crystallinity degree [30] and easy charge transport [31]. In the same way, hc-g-C_3N_4's low specific surface area and narrow electronic storage cause limited sensor applications [32]. In order to increase its catalysis activity, co-catalysts formation is one of the effective methods [33]. Hence, the preparations of co-catalysts with high stability and low cost are significant for sensor applications. Carbon dots (CDs) as zero-dimensional nanomaterial are composed of graphitic sp^2 carbon with a size below 10 nm [30]. Owing to their excellent physical and chemical properties, non-toxicity, and electron transfer, CDs are generally utilized in catalysis application [34]. Furthermore, the functional groups on CDs' surface enable effective binding to nanomaterial/biomolecules. Thus, the composite formation between hc-g-C_3N_4 and CDs has two important functions: (i) the enhancement of specific surface area providing easy immobilization of biomolecules and (ii) the promotion of electron transfer improving sensor performance.

MXene has attracted important attention as a result of a new material group including nitrides and transition metal carbides [35, 36]. For instance, titanium carbide (Ti_3C_2) shows high metallic conductivity and good surface properties. This metallic conductivity provides surface heterojunctions between MXene and semiconductor interface [37]. This surface heterojunction is an electron reservoir to allow the separation potential. Furthermore, some surface terminations such as O, OH, and/or F formed by the etching process demonstrate important redox-active sites [38]. Because of these properties, Ti_3C_2 MXene as a co-catalyst shows significant sensor/catalysis performance [39, 40].

In recent years, $Cd_{0.5}Zn_{0.5}S$ as a semiconductor photocatalyst shows perfect light-harvesting potential [41]. Pure CdS has corrosion effect, resulting in recombination rate of charge carrier [42]. Because of this, the combination of CdS with ZnS to form $Cd_{0.5}Zn_{0.5}S$ can prevent its limited applications. Especially, owing to Zn^{2+} having ion radius of 0.074 nm smaller than Cd^{2+} (0.097 nm), stronger connection among atoms occurs and this situation increases CdS's stability and activity [43].

Herein, it was aimed to develop a unique sandwich-type electrochemical immunosensor based on $Cd_{0.5}Zn_{0.5}S$/d-$Ti_3C_2T_x$ MXene composite as signal amplificator and hc-g-C_3N_4@CDs as electrochemical sensor platform to be utilized for h-FABP detection. After the preparation of hc-g-C_3N_4@CDs by a facile calcination technique, the efficient immobilization of primary antibody was performed by π-π stacking interactions. Then, the hydrothermal treatment was carried out for the preparation of $Cd_{0.5}Zn_{0.5}S$/d-$Ti_3C_2T_x$ MXene composite. The high sensitivity together with a shorter detection time for h-FABP sensing was successfully achieved owing to the unsurpassed electrochemical features of the proposed immunosensor. Moreover, this work paves the way for early diagnosis of acute myocardial infarction, as well as a rational environmentally benign route for synthesizing of hc-g-C_3N_4@CDs and $Cd_{0.5}Zn_{0.5}S$/d-$Ti_3C_2T_x$ MXene with minimal waste.

Experimental

Materials

h-FABP standard solution, monoclonal primary antibody (h-FABP-Ab_1), monoclonal secondary antibody (h-FABP-Ab_2), alpha-fetoprotein (AFP), platelet-derived growth factor (PDGF-BB), cardiac troponin I (cTnI), bovine serum albumin (BSA), copeptin (COP), carcinoembryonic antigen (CEA), human immunoglobulin (IgG), myoglobin (MYG), cardiac

troponin T (cTnT), dicyandiamide (DCYA), citric acid (CA), ethylenediamine (EDAM), titanium aluminum carbide (MAX, Ti_3AlC_2) powder, tetrabutylammonium hydroxide (TBAOH), $Zn(Ac)_2.H_2O$, $Cd(Ac)_2.4H_2O$, and thioacetamide were acquired from Sigma-Aldrich. As supporting electrolyte and dilution buffer, 0.1-M phosphate-buffered saline (PBS) solution at pH of 7.0 was used.

Physicochemical and electrochemical characterization instruments

The surface morphologies of samples were investigated both by ZEISS EVO 50 SEM and JEOL 2100 TEM. The XRD patterns were recorded via Rigaku X-ray diffractometer using Cu-Kα radiation at $\lambda = 0.154$ nm. XPS and FTIR analysis were acquired by PHI 5000 Versa Probe and Bruker Tensor 27 FT-IR (with DTGS detector), respectively. Furthermore, to assess the electrochemical performance of the immunosensor, the electrochemical measurements including differential pulse voltammetry (DPV), CV, and EIS techniques were conducted on Gamry Reference 600 work-station (Gamry, USA).

Synthesis of nanocomposites

After the preparation of DCYA (4.0 g) solution in ultra-pure water (50.0 mL) under strong stirring for 90 min, the obtained solution was transferred into alumina crucible. Then, several Ni foams were added to the above solution. The crystallization of the solution including DCYA and Ni foams was performed at 75 °C for 15 h. After that, the crucible was transferred in a muffle furnace and heating treatment was carried out at 600 °C for 90 min. Finally, the obtained hc-g-C_3N_4 was treated with HCl solution (10.0 mol L^{-1}) to remove Ni foams two times. b-g-C_3N_4 was also prepared by thermal polycondensation of DCYA (4.0 g) in a muffle furnace at 600 °C for 90 min.

After the preparation of CA (2.0 g) aqueous solution in ultra-pure water (50.0 mL), EDAM (600.0 μL) was added to this solution and strongly stirred. The solution was transferred to a Teflon steel autoclave and the heating treatment was performed at 250 °C for 6 h. After cooling to 25 °C, the dialysis bag was utilized for the elimination of the impurities for 70 h. Lastly, CDs (1.0 mg mL^{-1}) were obtained and kept at 25 °C. hc-g-C_3N_4@CDs composite was prepared by adding DCYA (4.0 g) and CDs (10.0 mL, 1.0 mg mL^{-1}) into several Ni foams. Then, the same heating and Ni foams' removal were performed for obtaining of hc-g-C_3N_4@CDs composite.

hc-g-C_3N_4@CDs as electrochemical sensor platform with h-FABP-Ab_1 and h-FABP immobilizations

A typical three-electrode setup was utilized for electrochemical characterizations. The glassy carbon electrode (GCE), Ag/AgCl (saturated KCl), and platinum (Pt) wire electrodes were used as the working electrode, the reference electrode, and the counter electrode, respectively. Before electrochemical measurements, glassy carbon electrodes were polished according to our previous paper [44]. Then, hc-g-C_3N_4@CDs composite dispersion (30.0 μL) was dropped on the polished GCEs. After the removing treatment of solvent by IR lamp, hc-g-C_3N_4@CDs composite–modified GCE was prepared (hc-g-C_3N_4@CDs/GCE). Subsequently, the immobilization of h-FABP-Ab_1 was performed by dropping h-FABP-Ab_1 dispersion (20.0 μL, 50.0 μg mL^{-1}) on hc-g-C_3N_4@CDs/GCE at 37.0 °C for 20 min (h-FABP-Ab_1/hc-g-C_3N_4@CDs/GCE). Then, BSA (2.0% *w*/*v*) was incubated on h-FABP-Ab_1/hc-g-C_3N_4@CDs/GCE at 37.0 °C for 20 min to remove non-specific interactions (BSA/h-FABP-Ab_1/hc-g-C_3N_4@CDs/GCE). For h-FABP protein immobilization on BSA/h-FABP-Ab_1/hc-g-C_3N_4@CDs/GCE, various h-FABP proteins (0.01, 0.05, 0.10, 0.20, 0.50, and 1.00 pg mL^{-1}) were interacted separately with BSA/h-FABP-Ab_1/hc-g-C_3N_4@CDs/GCE for 20 min at 37.0 °C and tagged as h-FABP/BSA/h-FABP-Ab_1/hc-g-C_3N_4@CDs/GCE. Finally, h-FABP/BSA/h-FABP-Ab_1/hc-g-C_3N_4@CDs/GCE was stored in 0.1 M PBS (pH 7.0).

Preparation of d-$Ti_3C_2T_x$ MXene, $Cd_{0.5}Zn_{0.5}S$, and $Cd_{0.5}Zn_{0.5}S$/d-$Ti_3C_2T_x$ MXene composites

The purchased Ti_3AlC_2 MAX phase was subjected to etching treatment of aluminum layer in 6.0-M HCl/LiF solution at 30 °C for 20 h [39, 40, 45]. After collection of the etched MAX phases via an ultrasonic treatment, $Ti_3C_2T_X$ MXene dilution (20.0 mg mL^{-1}) in ultra-pure water was prepared. The obtained MXene was tagged as $Ti_3C_2T_x$ MXene (T_x is surface terminations such as O, OH, and/or F). After the strong stirring of multilayered $Ti_3C_2T_X$ MXene in TBAOH solution (10.0 mg mL^{-1}, 15.0 mL) at 25 °C for 25 h, the centrifugation was carried out at 15000 rpm. The collected $Ti_3C_2T_X$ MXene was washed in ultra-pure water to remove TBAOH residues. After that, the collected $Ti_3C_2T_X$ MXene was subjected to ultrasonic treatment for 45 min, providing delaminated $Ti_3C_2T_x$ MXene (d-$Ti_3C_2T_X$ MXene) [46].

Following the preparation of aqueous solution including in $Zn(Ac)_2.H_2O$ (10.0 mmol) and $Cd(Ac)_2.4H_2O$ (10.0 mmol), thioacetamide (30.0 mmol) and EDAM (15.0 mL) were added into this aqueous solution under vigorous stirring during 45 min. Afterward, the as-obtained mixture was placed to a Teflon-lined autoclave and heat treatment was conducted at 200 °C. Finally, as-obtained $Cd_{0.5}Zn_{0.5}S$ was washed with ultra-pure water, followed by drying overnight.

For the preparation of composites, firstly, aqueous solution including $Zn(Ac)_2.H_2O$ (10.0 mmol) and

$Cd(Ac)_2.4H_2O$ (10.0 mmol) was prepared. After that, thioacetamide (30.0 mmol) and d-$Ti_3C_2T_X$ MXene were added into the above aqueous solution under argon atmosphere for 90 min. A series of $Cd_{0.5}Zn_{0.5}S$/x wt% d-$Ti_3C_2T_x$ MXene (x: 1, 3, 5, and 7) was prepared with altering the amount of d-$Ti_3C_2T_X$ MXene. After that, the prepared series was subjected to hydrothermal treatment at 180 °C for 20 h. After centrifugation treatment, $Cd_{0.5}Zn_{0.5}S$/x wt% d-$Ti_3C_2T_x$ MXene was collected and dried overnight.

$Cd_{0.5}Zn_{0.5}S$/d-$Ti_3C_2T_x$ MXene as signal amplificator with h-FABP-Ab_2 conjugation

Firstly, h-FABP-Ab_2 dispersion (20.0 μL, 50.0 μg mL^{-1}) was prepared and conjugated to $Cd_{0.5}Zn_{0.5}S$/d-$Ti_3C_2T_x$ MXene via magnetic stirring at 37.0 °C for 20 min. Afterward, the Ab_2 bioconjugates ($Cd_{0.5}Zn_{0.5}S$/d-$Ti_3C_2T_x$ MXene/h-FABP-Ab_2) were collected by centrifuging at 5000 rpm for 40 min.

Electrochemical measurements

Sandwich-type electrochemical immunosensor was prepared by antibody-antigen interactions between h-FABP/BSA/h-FABP-Ab_1/hc-g-C_3N_4@CDs/GCE and $Cd_{0.5}Zn_{0.5}S$/d-Ti_3C_2Tx MXene/h-FABP-Ab_2. $Cd_{0.5}Zn_{0.5}S$/d-Ti_3C_2Tx MXene/h-FABP-Ab_2 dispersion (20.0 μL, 10.0 mg mL^{-1}) was dropped on h-FABP/BSA/h-FABP-Ab_1/hc-g-C_3N_4@CDs/GCE at the immune reaction time of 20 min. Lastly, the final version of the developed immunosensor was dried at 25.0 °C and stored in 0.1 M PBS (pH 7.0, 2.0 mL) for 30 min. After that, the developed immunosensor such as working electrode was used for electrochemical measurements in 0.1 M PBS (pH 7.0, 2.0 mL) containing 1.0-mM H_2O_2 solution. All electrochemical measurements were conducted in argon-saturated electrolyte. After the application of the potential scan in the range of +0.1/+0.5 V for DPV measurements, the voltammograms at +0.30 V were evaluated. Scheme 1 demonstrated the preparation procedures such as hc-g-C_3N_4@CDs, $Cd_{0.5}Zn_{0.5}S$/d-$Ti_3C_2T_x$ MXene, the immobilizations of proteins, and the final electrochemical immunosensor.

Sample preparation

h-FABP free plasma samples were supplied from Blood Bank in TURKEY. Sample preparation protocol was explained in detail on Supplemantary Data [47].

Results and discussion

Principle of electrochemical h-FABP immunosensor based on $Cd_{0.5}Zn_{0.5}S$/d-$Ti_3C_2T_x$ MXene and hc-g-C_3N_4@CDs

In this study, electrochemical h-FABP immunosensor based on core-shell high-crystalline graphitic carbon nitride@carbon dots as sensor platform and $Cd_{0.5}Zn_{0.5}S$/d-$Ti_3C_2T_x$ MXene as signal amplificator was prepared. A facile calcination tecnique was applied to the preparation of hc-g-C_3N_4@CDs. However, van der Waals interactions between carbon-nitrogen layers in hc-g-C_3N_4 can prevent charge transfer, causing some limitations on sensor performance. Hence, provided that surface heterojunctions are created, this sensor performance can be enhanced. In this study, the surface heterojunctions between hc-g-C_3N_4 and CDs were formed by π-π stacking interactions, providing the efficient immobilization of h-FABP-Ab_1 [48].

In the preparation process of signal amplificator, d-$Ti_3C_2T_X$ MXene was firstly introduced into $Zn(Ac)_2.H_2O$ and $Cd(Ac)_2.4H_2O$ aqueous solutions. Then, Cd^{2+} and Zn^{2+} ions started to efficiently adsorb on T_x (O, OH, and/or F) terminations on MXene structure and thioacetamide as sulfur source was coordinated with Cd^{2+} and Zn^{2+} ions. After the conversion of fluorine terminations in d-$Ti_3C_2T_x$ MXene into oxygen/hydroxyl terminations and the decomposition of thioacetamide during hydrothermal treatment, S^{2-} anions were released and these released S^{2-} anions were again coordinated with Cd^{2+} and Zn^{2+} ions on MXene surface, providing growth of $Cd_{0.5}Zn_{0.5}S$ on d-$Ti_3C_2T_x$ MXene. Thanks to strong π-π and electrostatic interactions between h-FABP-Ab_2 and $Cd_{0.5}Zn_{0.5}S$/d-$Ti_3C_2T_x$ MXene, a novel electrochemical h-FABP immunosensor having high stability was prepared. Lastly, the performance of electrochemical h-FABP immunosensor was monitored using H_2O_2 as redox probe which converted into O_2 at about +0.30 V [49].

Characterizations of d-$Ti_3C_2T_x$ MXene and $Cd_{0.5}Zn_{0.5}S$/d-$Ti_3C_2T_x$ MXene composites

Firstly, SEM images of Ti_3AlC_2 MAX and d-$Ti_3C_2T_x$ MXene were demonstrated in Fig. S1. According to SEM image of Ti_3AlC_2 MAX (Fig. S1A), the bulk and cluster particles were observed. However, after etching of aluminum from Ti_3AlC_2 MAX phase, the delaminated and homogeneous structure was obtained (Fig. S1B). Hence, this delaminated formation prevents agglomeration, providing the formation of cluster particles. Figure 1a also shows the XRD patterns of Ti_3AlC_2 MAX and d-$Ti_3C_2T_x$ MXene. The XRD peaks at 9.23°, 18.13°, and 38.12° relating to (002), (004), and (104) planes confirmed the presence of Ti_3AlC_2 MAX, respectively [49]. Nonetheless, XRD peak at 38.12° belonging to Ti_3AlC_2 MAX completely

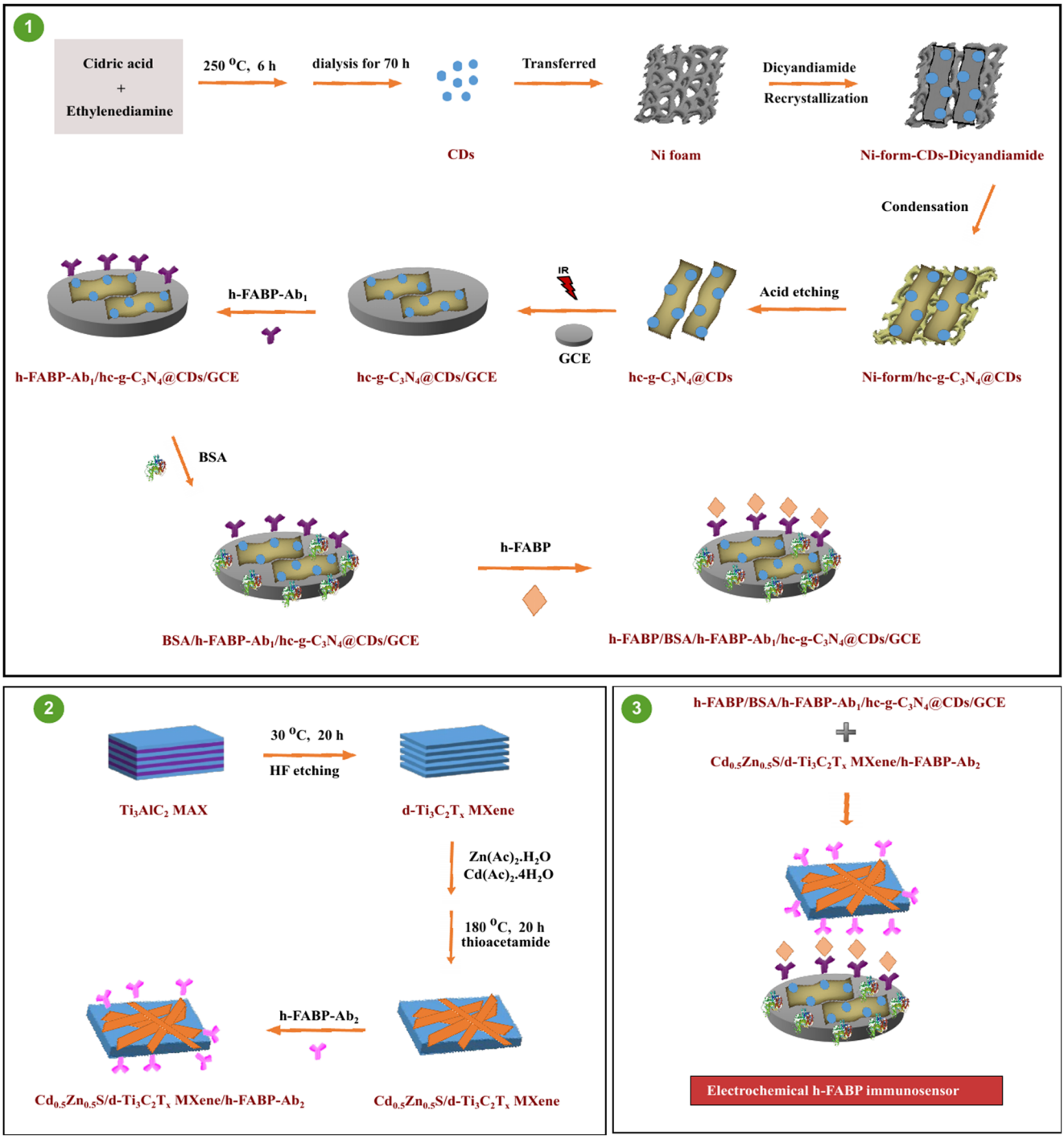

Scheme 1 Preparation procedure of voltammetric h-FABP immunosensor

disappeared for d-$Ti_3C_2T_x$ MXene. Moreover, XRD peaks at 9.23° and 18.13° belonging to Ti_3AlC_2 MAX got wider at smaller angles owing to interlayer spacing expansion, confirming the successful preparation of d-$Ti_3C_2T_x$ MXene [50]. In addition, the presence of T_x groups (O, OH, and/or F) on XPS spectrum of d-$Ti_3C_2T_X$ MXene verified the fluorine-terminated structure of d-$Ti_3C_2T_X$ MXene (Fig. S2A) and the observed absorption peaks at 267 nm and 773 nm for optical properties of d-$Ti_3C_2T_X$ MXene confirmed the successful synthesis of delaminated MXene (Fig. S2B) [40]. Raman spectra (Fig. S3) were recorded for Ti_3AlC_2 MAX and d-$Ti_3C_2T_X$ MXene. According to Raman spectrum of Ti_3AlC_2 MAX, the peaks a and b were attributed to Al–Ti vibrations and the peaks c and d were corresponded to Ti–C vibrations [51]. However, peaks a and b almost disappeared, whereas the intensities of peaks c and d became weaker after

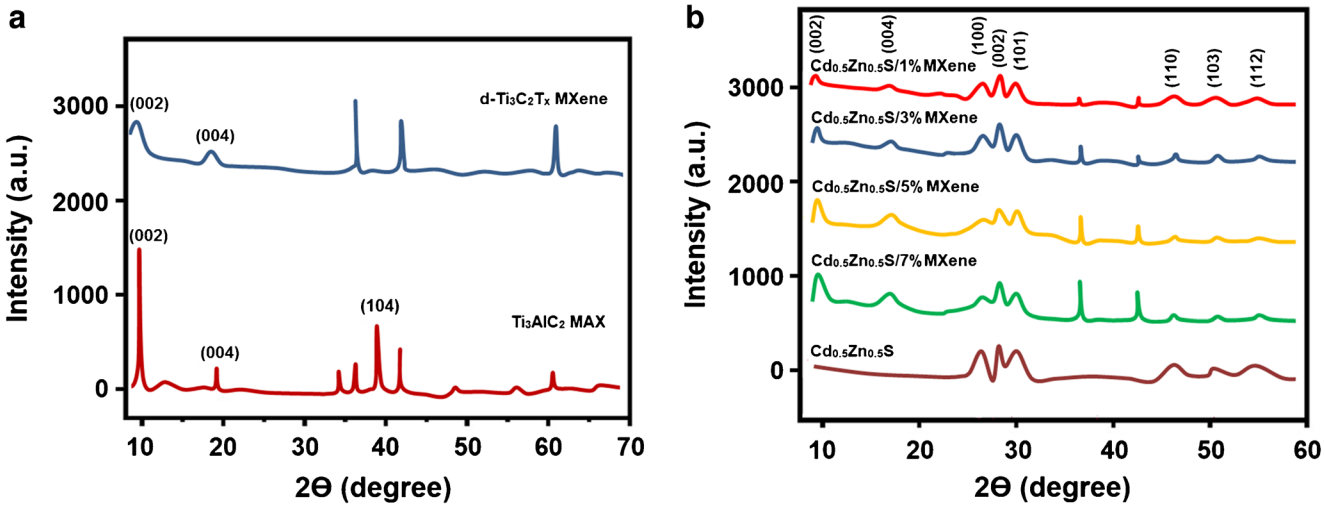

Fig. 1 **a** XRD patterns of Ti_3AlC_2 MAX and d-$Ti_3C_2T_x$ MXene. **b** XRD patterns of $Cd_{0.5}Zn_{0.5}S$ and all prepared composites including different amounts of MXene

etching treatment. The disappearance of peaks a and b showed the successful etching treatment of Ti_3AlC_2 MAX, providing the formation of d-$Ti_3C_2T_X$ MXene. Nonetheless, the weak peak intensities in relation to peaks c and d were corresponded to Ti–C vibrations owing to MXene's thinner layer [52]. According to Fig. 1b, XRD peaks at 25.93°, 27.58°, 29.27°, 38.39°, 46.17°, 49.97°, and 54.45° were corresponded to (100), (002), (001), (102), (110), (103), and (112) planes of $Cd_{0.5}Zn_{0.5}S$, respectively (Fig. 1b). The majority of specific bands relating to $Cd_{0.5}Zn_{0.5}S$ and d-$Ti_3C_2T_x$ MXene on XRD patterns of all prepared composites including different amounts of MXene was observed. For instance, XRD peaks at 9.23° and 18.13° belonging to d-$Ti_3C_2T_X$ MXene were observed on all $Cd_{0.5}Zn_{0.5}S$/d-$Ti_3C_2T_x$ MXene composites and the intensities of these peaks at 9.23° and 18.13° increased in proportion to the amount of d-$Ti_3C_2T_X$ MXene.

Figure 2a demonstrates TEM image of $Cd_{0.5}Zn_{0.5}S$, suggesting an obvious aggregation with a mean particle size of 20–25 nm. According to SEM (Fig. 2b) and TEM (Fig. 2c) analysis of $Cd_{0.5}Zn_{0.5}S$/7wt%d-$Ti_3C_2T_x$ MXene, the rod-like morphology of composite was observed. Finally, HRTEM image (Fig. 2d) indicated the crystal structures of $Cd_{0.5}Zn_{0.5}S$ and d-$Ti_3C_2T_x$ MXene having 0.318 nm [53] and 0.259 nm [54], respectively.

Then, XPS analysis (Fig. S4) was performed to show the bonding states and chemical compositions of $Cd_{0.5}Zn_{0.5}S$/7wt%d-$Ti_3C_2T_x$ MXene composite. According to XPS survey spectra (Fig. S4A), Ti, C, Cd, Zn, S, and O elements' presence suggested that the fluorine-terminated d-$Ti_3C_2T_X$ MXene was successfully converted to oxygen-terminated d-$Ti_3C_2T_X$ MXene after hydrothermal treatment [55]. Ti2p's high-resolution XPS spectrum showed (Fig. S4B) that the peaks at 464.58, 459.93, 458.08, and 454.86 eV were attributed to Ti-O ($2p_{1/2}$), Ti-C ($2p_{1/2}$), Ti-O ($2p_{3/2}$) and Ti-C ($2p_{3/2}$), respectively [53]. According to C1s high-resolution XPS spectrum (Fig. S4C), the peaks at 285.10 and 286.18 eV were corresponded to C–C and the C–O bonds, respectively. In addition, the specific peaks at 287.94 and 280.89 eV were attributed to O–C=O and C–Ti, respectively [56]. For Cd3d high-resolution spectrum (Fig. S4D), the peaks at 404.91 and 412.05 eV relating to $Cd3d_{5/2}$ and $Cd3d_{3/2}$, respectively, demonstrated the valence state (2+) of cadmium element. Figure S4E indicated S2p high-resolution spectrum at 162.05 and 163.07 eV, providing $S2p_{3/2}$ and $S2p_{1/2}$ of S^{2-}, respectively [57]. Finally, Zn2p high-resolution spectrum demonstrated two peaks at 1021.87 and 1045.07 eV corresponding to $Zn2p_{3/2}$ and $Zn2p_{1/2}$, respectively (Fig. S4F) [58]. Hence, XPS results confirmed the successful synthesis of $Cd_{0.5}Zn_{0.5}S$/oxygen-terminated d-$Ti_3C_2T_X$ MXene composite.

Characterizations of hc-g-C_3N_4, bulk-g-C_3N_4 (b-g-C_3N_4), CDs, and hc-g-C_3N_4@CDs composite

XRD patterns (Fig. 3a) were obtained for the investigation of the crystal structures of hc-g-C_3N_4, b-g-C_3N_4 and hc-g-C_3N_4@CDs composite. According to XRD pattern of b-g-C_3N_4, two different peaks at 13.1° and 27.1° were observed, suggesting (100) and (002) crystallographic planes of g-C_3N_4, respectively. This situation corresponds to aromatic systems' in-plane structural packing and interlayer superposition reflection [59]. For hc-g-C_3N_4, a similar pattern with higher angles was obtained. However, the intensity of the peak corresponding to (002) plane increased in comparison with b-g-C_3N_4 owing to the increases of condensation/crystallization and the decrease of interfacial space [60]. In addition, the peak at 25.8° was attributed to the typical peak of carbon materials on XRD pattern of CDs (Fig. S5A) [61]. For XRD pattern of hc-g-C_3N_4@CDs composite, the obvious peak at 25.8° related to CDs appeared, confirming the successful synthesis of hc-g-

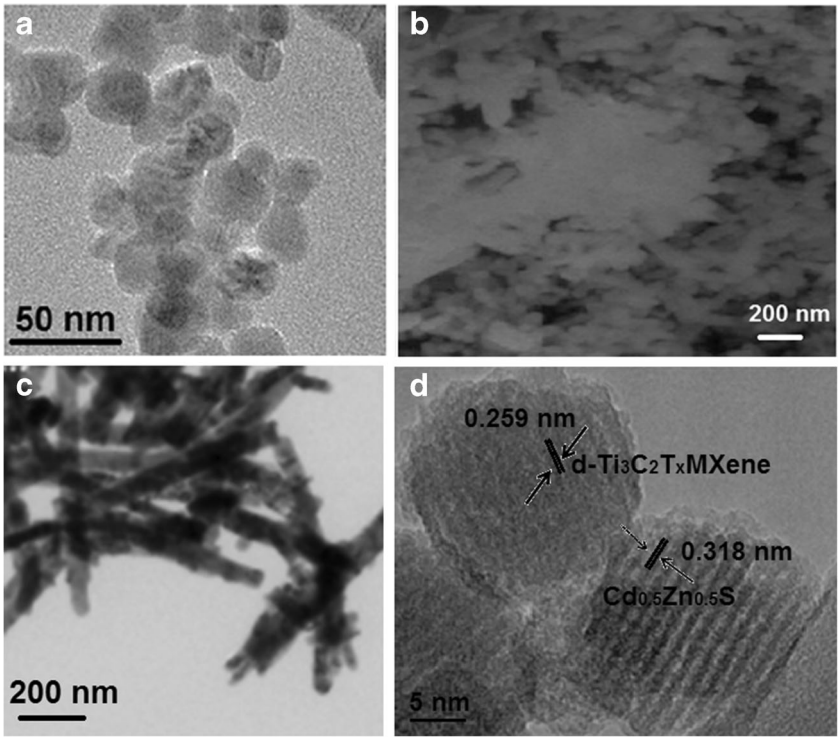

Fig. 2 **a** TEM image of $Cd_{0.5}Zn_{0.5}S$. **b** SEM image and **c** TEM image of $Cd_{0.5}Zn_{0.5}S$/7wt%d-$Ti_3C_2T_x$ MXene. **d** HRTEM image of $Cd_{0.5}Zn_{0.5}S$/7wt%d-$Ti_3C_2T_x$ MXene

C_3N_4@CDs composite. FTIR spectra were obtained for hc-g-C_3N_4 and hc-g-C_3N_4@CDs composite (Fig. 3b). The absorption bands on 3000–3400 cm^{-1}, 1100–1650 cm^{-1}, and 810 cm^{-1} were corresponded to O–H/N–H stretching, CN heterocycle stretching, and heptazine stretching on FTIR spectrum of hc-g-C_3N_4, respectively. The peaks at 3450 and 1629 cm^{-1} were attributed to –OH and –C=O groups' stretching, respectively on FTIR spectrum of CDs (Fig. S5B) [62]. Especially, on FTIR spectrum of hc-g-C_3N_4@CDs composite, similar typical absorption peaks confirmed that basic structure was preserved without any changes after the incorporation of carbon dots into hc-g-C_3N_4.

XPS analysis (Fig. 4) was carried out to determine chemical compositions of hc-g-C_3N_4@CDs composite. According to Fig. 4a, C, N, and O elements' presence demonstrated the successful synthesis of hc-g-C_3N_4@CDs composite. The peaks at 284.12, 285.95, and 287.91 eV on C1s spectrum were corresponded to graphite sp^2 C–C bonds [63], sp^2 C atoms of s-triazine rings attached to NH groups (C-NH_x) [64], and sp^2 C atoms bonded to N in aromatic ring (N-C=N) [65], respectively. On N1s spectrum (Fig. 4b), the peaks at 398.23, 400.08, 401.27, and 403.93 eV were attributed to sp^2 N atoms on C-N=C group, sp^3 N atoms on H-N-$(C)_3$ group, NH groups, and the effect of charge (Fig. 4c) [66]. Finally, the peaks at 531.23, 532.69, and 534.13 eV were attributed to O–H, C–O, and C=O, respectively on O1s spectrum (Fig. 4d). Hence, these peaks confirmed oxygen-containing functional groups of carbon dots [67].

Specific surface areas of hc-g-C_3N_4 and hc-g-C_3N_4@CDs were obtained by N_2 adsorption-desorption isotherms (Fig. S6). Brunauer Emmett Teller (BET) plots demonstrated type IV isotherm for hc-g-C_3N_4 and hc-g-C_3N_4@CDs, indicating

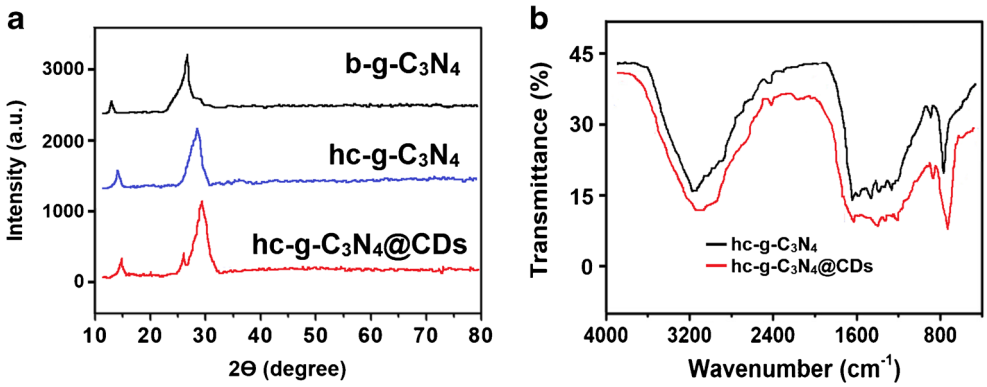

Fig. 3 **a** XRD patterns of hc-g-C_3N_4, b-g-C_3N_4 and hc-g-C_3N_4@CDs composite. **b** FTIR spectra of hc-g-C_3N_4 and hc-g-C_3N_4@CDs composite

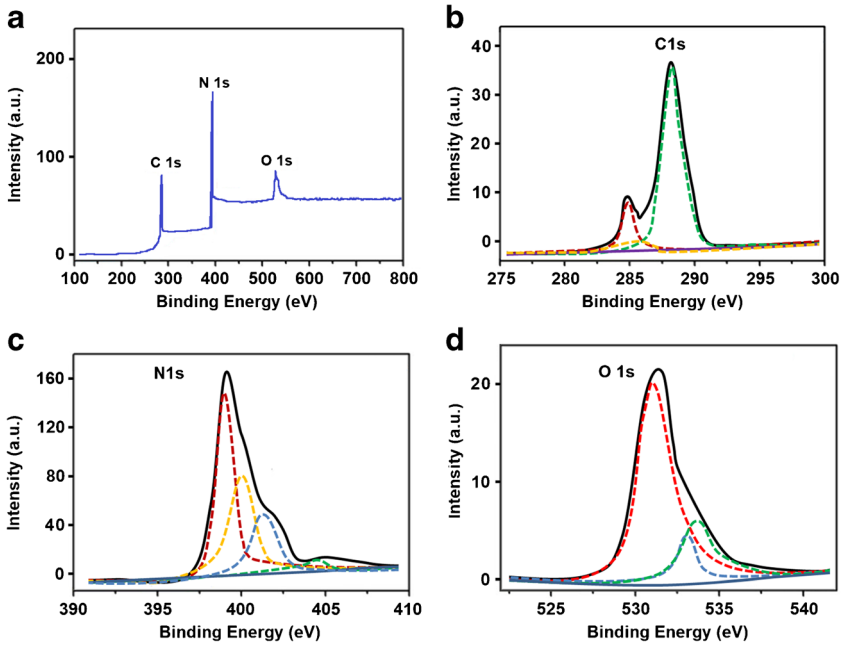

Fig. 4 **a** XPS survey spectrum of hc-g-C_3N_4@CDs composite and high-resolution XPS spectra of **b** C1s, **c** N1s, and **d** O1s

the formation of mesoporous material [68]. BET values were calculated as 20.4 and 32.19 $m^2\ g^{-1}$ for hc-g-C_3N_4 and hc-g-C_3N_4@CDs, respectively. These results showed that hc-g-C_3N_4@CDs composite with larger specific surface area provides more efficient immobilization capacity and surface-active areas for sensor applications.

Finally, TEM and HRTEM images of hc-g-C_3N_4@CDs were obtained to investigate the microstructure of hc-g-C_3N_4@CDs (Fig. 5). Hence, two-dimensional nanosheet structure of composite is shown in Fig. 5a. In addition, according to Fig. 5b with different magnification, the uniform incorporation of CDs on hc-g-C_3N_4 was observed. According to HRTEM images (Fig. 5c and d), the interplanar spaces of 0.22 nm and 0.34 nm attributing to (100) and (002) planes for CDs and hc-g-C_3N_4, respectively, were obtained. Thus, the successful dispersion of CDs on hc-g-C_3N_4 was confirmed.

Electrochemical characterizations of sensor platform and signal amplificator

The CV measurements were conducted in 1.0-mM $[Fe(CN)_6]^{3-}$ solution containing 0.1 M KCl to characterize the electrochemical sensor platform behavior of hc-g-C_3N_4@CDs composite (Fig. 6a). As can be seen in "*Curve a*" obtained for bare GCE, the anodic and the cathodic peaks were appeared at around +0.50 V and + 0.25 V, respectively. After the modification of GCE with hc-g-C_3N_4, these anodic/cathodic peaks became more evident as a result of high crystallinity structure of hc-g-C_3N_4 and easy charge transport (curve b) [31]. Lastly, when hc-g-C_3N_4@CDs-modified GCE was used, higher peak currents and smaller peak potential difference ($\Delta Ep = Epa - Epc$) were observed on curve c owing to CDs' good chemical stability and fast electron transfer. In addition, CDs' oxygen-containing functional groups providing larger surface area contributed to this electrocatalytic effect [69]. Then, the important electrocatalytic decreases occurred after primer antibody's immobilization on curve d due to the ability of electron transfer blocking of primer antibody. Moreover, more electrocatalytic decreases were observed after BSA incubation (curve e) and h-FABP protein immobilization (curve f). Hence, we can say that the decorations of primer antibody, BSA, and h-FABP protein to hc-g-C_3N_4@CDs/GCE were succesfully carried out for sensor platform development.

To verify CV results, EIS measurements are recorded in Fig. 6b. After modification of GCE with hc-g-C_3N_4 and CDs, the obvious electrical conductivities increased, showing easier electron transfer (curves b and c on Fig. 6b). In the same way, the incorporations of primer antibody, BSA, and h-FABP protein to hc-g-C_3N_4@CDs/GCE resulted in electrode resistance increases (curved, e, and f on Fig. 6b). Finally, both CV and EIS measurements confirmed the successful sensor platform construction with primer antibody, BSA, and h-FABP protein.

For the investigation of electrocatalytic effects of a series of $Cd_{0.5}Zn_{0.5}S$/x wt% d-$Ti_3C_2T_x$ MXene (x: 1, 3, 5 and 7) composites on the developed immunosensor performance, EIS graphs of $Cd_{0.5}Zn_{0.5}S$/1wt%d-$Ti_3C_2T_x$MXene/GCE, $Cd_{0.5}Zn_{0.5}S$/3wt%d-$Ti_3C_2T_x$MXene/GCE, $Cd_{0.5}Zn_{0.5}S$/5wt%d-$Ti_3C_2T_x$MXene/GCE, and $Cd_{0.5}Zn_{0.5}S$/7wt%d-$Ti_3C_2T_x$MXene/GCE were obtained (Fig. 6c). According to EIS graphs, since the electron transfer resistance on $Cd_{0.5}Zn_{0.5}S$/7wt%d-$Ti_3C_2T_x$MXene/GCE is the lowest, the best electrocatalytic effect occurs on $Cd_{0.5}Zn_{0.5}S$/7wt%d-

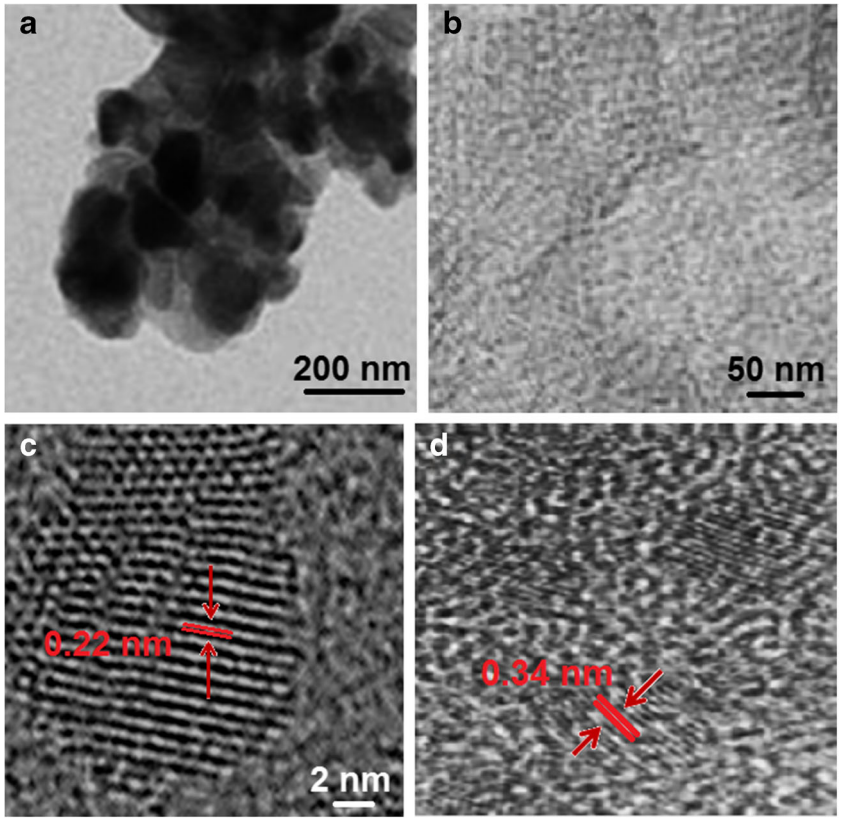

Fig. 5 **a** TEM and **b** TEM with different magnification images. **c**, **d** HRTEM images of hc-g-C_3N_4@CDs composite

$Ti_3C_2T_x$MXene/GCE. Thus, we selected $Cd_{0.5}Zn_{0.5}S$/7wt%d-$Ti_3C_2T_x$MXene composite for the preparation of signal amplificator in this study. Also, the experimental data were fitted to standard randles equivalent circuit including solution resistance (Rs), charge transfer resistance (Rct), and constant phase element (CPE) for $Cd_{0.5}Zn_{0.5}S$/x wt% d-$Ti_3C_2T_x$ MXene (x: 1, 3, 5, and 7) composites.

In addition, for characterization of the prepared signal amplificator step-by-step, various electrochemical immunosensors including different signal amplificators such as 7wt%d-$Ti_3C_2T_x$MXene and $Cd_{0.5}Zn_{0.5}S$/7wt%d-$Ti_3C_2T_x$MXene were prepared and DPV measurements were performed (Fig. 6d). For this aim, FABP/BSA/h-FABP-Ab_1/hc-g-C_3N_4@CDs/GCE was seperately exposed to an immune reaction of 20 min with h-FABP-Ab_2, 7wt%d-$Ti_3C_2T_x$MXene/h-FABP-Ab_2, and $Cd_{0.5}Zn_{0.5}S$/7wt%d-$Ti_3C_2T_x$MXene/h-FABP-Ab_2. DPV measurements were performed in 1.0 mM H_2O_2 in pH 7.0, 0.1 M PBS, and in the absence of H_2O_2. Owing to $Ti_3C_2T_x$MXene's high metallic conductivity, efficient charge-carrier transfer, redox activation sites, and good surface properties [38, 40, 49], more electrocatalytic effect occurred on curve c in comparison with curve b. Finally, due to significant catalysis effect of $Cd_{0.5}Zn_{0.5}S$ [41] and important synergistic effect between $Cd_{0.5}Zn_{0.5}S$ and 7wt%d-$Ti_3C_2T_x$MXene, the higher current signals (curve d) on $Cd_{0.5}Zn_{0.5}S$/7wt%d-$Ti_3C_2T_x$MXene/h-FABP-Ab_2 were found in comparison with 7wt%d-$Ti_3C_2T_x$MXene/h-FABP-Ab_2. In addition, the specific surface areas of developed immunosensors were calculated as 0.170 ± 0.04 cm^2 for bare GCE, 0.389 ± 0.03 cm^2 for h-FABP-Ab_2/h-FABP/BSA/h-FABP-Ab_1/hc-g-C_3N_4@CDs/GCE, 0.607 ± 0.01 cm^2 for 7wt%d-$Ti_3C_2T_x$MXene/h-FABP-Ab_2/h-FABP/BSA/h-FABP-Ab_1/hc-g-C_3N_4@CDs/GCE, and 0.917 ± 0.03 cm^2 for $Cd_{0.5}Zn_{0.5}S$/7wt%d-$Ti_3C_2T_x$MXene/h-FABP-Ab_2/h-FABP/BSA/h-FABP-Ab_1/hc-g-C_3N_4@CDs/GCE in the presence of 1.0-mM $[Fe(CN)_6]^{3-}$ solution by the equation (Randles–Sevcik) of $i_p = 2.69 \times 10^5\ A\ n^{3/2}\ D^{1/2}\ C\ v^{1/2}$, where i_p was the current, C (mol cm^{-3}) was $[Fe(CN)_6]^{3-}$ concentration, v was the scan rate (10–500 mV s^{-1}), and A was surface area (cm^2) ($n = 1$, $D = 7.6 \times 10^{-6}$ cm^2 s^{-1} for $[Fe(CN)_6]^{3-}$) [47]. Thus, $Cd_{0.5}Zn_{0.5}S$/7wt%d-$Ti_3C_2T_x$MXene/h-FABP-Ab_2 was preferred for subsequent immunosensor applications.

Optimization for electrochemical measurements

The detailed evaluation of the effect of solution pH, immune reaction time, and the concentration of H_2O_2 and $Cd_{0.5}Zn_{0.5}S$/d-$Ti_3C_2T_x$ MXene/h-FABP-Ab_2 solution was depicted in Fig. S7.

Linearity range

h-FABP as a marker of cardiac muscle cell damage is a low–molecular weight (15,000 Da) protein and is abundant in the

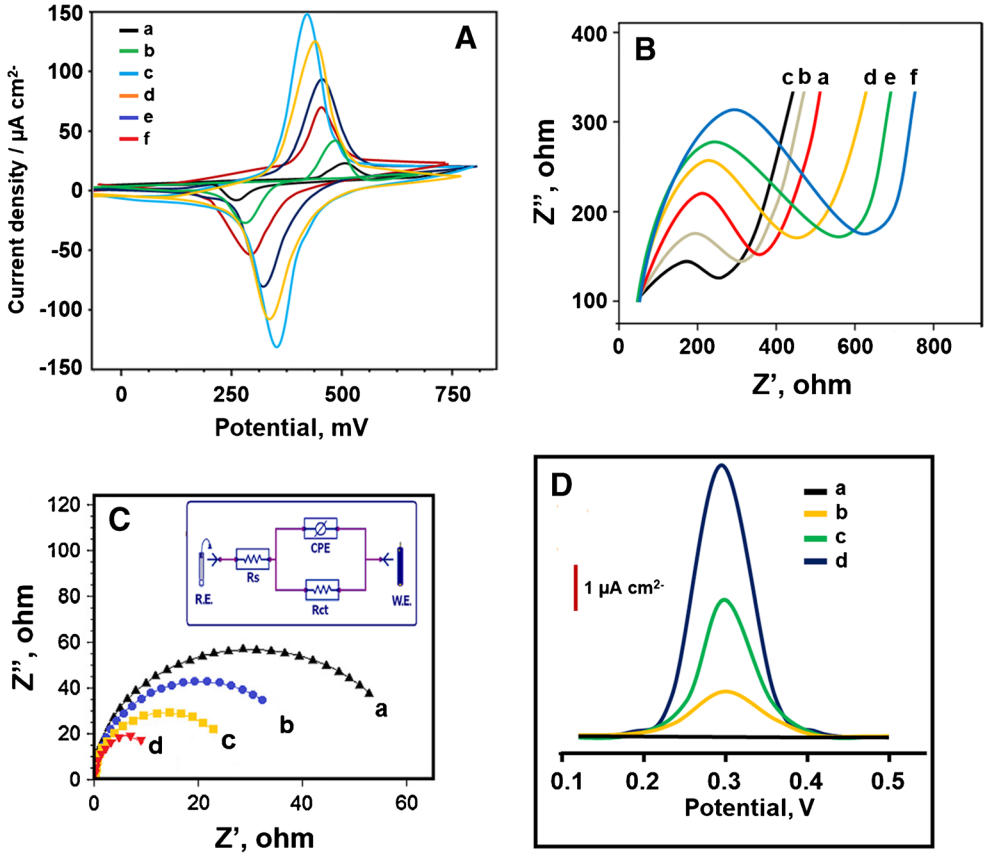

Fig. 6 **a** Cyclic voltammograms. **b** EIS reponses at (a) bare GCE, (b) hc-g-C_3N_4/GCE, (c) hc-g-C_3N_4@CDs/GCE, (d) h-FABP-Ab_1/hc-g-C_3N_4@CDs/GCE, (e) BSA/h-FABP-Ab_1/hc-g-C_3N_4@CDs/GCE, and (f) h-FABP/BSA/h-FABP-Ab_1/hc-g-C_3N_4@CDs/GCE (scan rate of 50 mV s^{-1}) in 1.0 mM $[Fe(CN)_6]^{3-}$ containing 0.1 M KCl. **c** EIS reponses at (a) $Cd_{0.5}Zn_{0.5}S$/1wt%d-$Ti_3C_2T_x$MXene/GCE, (b) $Cd_{0.5}Zn_{0.5}S$/3wt%d-$Ti_3C_2T_x$MXene/GCE, (c) $Cd_{0.5}Zn_{0.5}S$/5wt%d-$Ti_3C_2T_x$MXene/GCE, and (d) $Cd_{0.5}Zn_{0.5}S$/7wt%d-$Ti_3C_2T_x$MXene/GCE in 1.0 mM $[Fe(CN)_6]^{3-}$ containing 0.1 M KCl. Inset: Randles equivalent circuit. **d** DPV responses of the proposed immunosensors incubated with 0.10 pg mL^{-1} FABP protein by h-FABP-Ab_2/h-FABP/BSA/h-FABP-Ab_1/hc-g-C_3N_4@CDs/GCE (curve b), 7wt%d-$Ti_3C_2T_x$MXene/h-FABP-Ab_2/h-FABP/BSA/h-FABP-Ab_1/hc-g-C_3N_4@CDs/GCE (curve c), and $Cd_{0.5}Zn_{0.5}S$/7wt%d-$Ti_3C_2T_x$MXene/h-FABP-Ab_2/h-FABP/BSA/h-FABP-Ab_1/hc-g-C_3N_4@CDs/GCE (curve d) in absence of H_2O_2 (curve a) and in presence of 1.0 mM H_2O_2

cardiac muscle cell cytoplasm. Serum and pericardial fluid levels of h-FABP were obtained as 0.0–10.0 ng mL^{-1} and 0.0–20.0 ng mL^{-1}, respectively in literature [70]. In this study, electrochemical signals linearly increased with h-FABP concentrations from 0.01 to 1.00 pg mL^{-1} (Fig. 7). The equation of linear regression was y (I, µA cm^{2-}) = 44.42x (h-FABP concentration, pg mL^{-1}) + 0.029 with correlation coefficient of R^2 = 0.9985. By means of Eq. (1) and Eq. (2), the quantification limit (LOQ) and the detection limit values were obtained as 0.01 pg mL^{-1} and 3.30 fg mL^{-1}, respectively.

$$\mathrm{LOQ} = 10.0\ S/m \quad (1)$$

$$\mathrm{LOD} = 3.3\ S/m \quad (2)$$

where S is the standard deviation of intercept and m is the slope of calibration equation. Hence, this calibration range showed that h-FABP level can be followed easily in cases not only by AMI, but also by AMI related to sensitive myocardial ischemia. Moreover, the developed electrochemical h-FABP immunosensor demonstrated superior sensitivity in comparison with other analytical techniques (Table 1). This was attributed to $Ti_3C_2T_x$MXene's high metallic conductivity and catalysis effect of $Cd_{0.5}Zn_{0.5}S$. In addition, as a result of the preparation of $Cd_{0.5}Zn_{0.5}S$/7wt%d-$Ti_3C_2T_x$ MXene composite via hydrothermal synthesis, it can be suggested that this work offered an environmentally benign immunosensor design by means of little waste generation.

Recovery

Recovery values of h-FABP in the presence of pH 7.0, 0.1 M PBS containing 1.0 mM H_2O_2 were presented on Table S1. These values were calculated by the Eq. (3) below:

$$\mathrm{Recovery} = \mathrm{Found\ h{-}FABP,\ pg\ mL^{-1}} / \mathrm{Theoretical\ h{-}FABP,\ pg\ mL^{-1}} \quad (3)$$

According to Table S1 relating to the close values to 100.00%, the other agents such as PDGF-BB, AFP, cTnI, BSA, COP, CEA, IgG, MYG, and cTnT in plasma samples

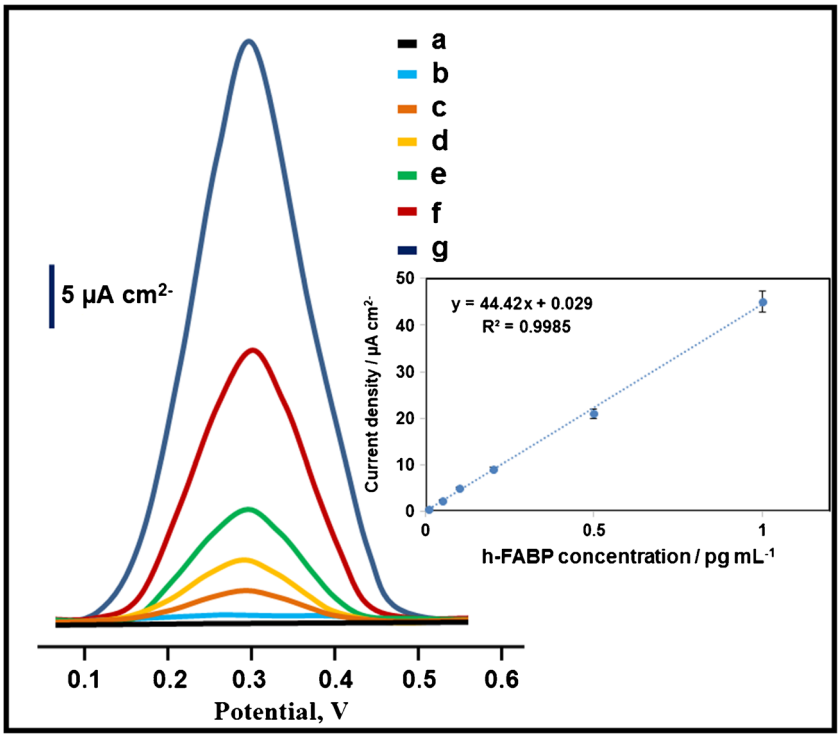

Fig. 7 Concentration effect on immunosensor signals: (a) blank, (b) 0.01 pg mL^{-1} h-FABP, (c) 0.05 pg mL^{-1} h-FABP, (d) 0.10 pg mL^{-1} h-FABP, (e) 0.20 pg mL^{-1} h-FABP, (f) 0.50 pg mL^{-1} h-FABP, (g) 1.0 pg mL^{-1} h-FABP. Inset: Calibration curve for electrochemical h-FABP immunosensor (potential range is +0.1/+0.5 V; parameters are frequency of 50 Hz, pulse amplitude of 20 mV, and scan increment of 3 mV)

cannot negatively affect accurate and selective determination of h-FABP. In addition, standard addition method was applied to plasma samples to investigate high selectivity of electrochemical h-FABP immunosensor and calibration equation of standard addition method was found to be y (I, µA cm^{2-}) = 44.49x (h-FABP concentration, pg mL^{-1}) + 0.174. Thus, the close slopes between the standard addition method and linear regression method confirmed that the prepared electrochemical immunosensor selectively detected h-FABP protein in plasma samples.

EIS technique was carried out in order to evaluate the validity of the electrochemical immunosensor [21]. Table S2 demonstrates the results obtained by the two different techniques for h-FABP detection. The compared results showed that no important difference was found between the electrochemical immunosensor and EIS ($T_{calculated} > T_{tabulated}$, $p > 0.05$).

Selectivity, stability, reproducibility, and reusability of the prepared h-FABP immunosensor

In order to investigate the selectivity of prepared h-FABP immunosensor, ten protein solution mixtures including h-FABP, h-FABP+PDGF-BB, h-FABP+AFP, h-FABP+cTnI, h-FABP+BSA, h-FABP+COP, h-FABP+CEA, h-FABP+IgG, h-FABP+MYG, and h-FABP+cTnT were separately prepared. After the development of ten electrochemical immunosensors by these 10 protein solutions, these immunosensors were applied to 1.0-mM H_2O_2 solution including in pH 7.0, 0.1 M PBS (2.0 mL). Figure 8a demonstrates 0.23% of relative standard deviation (RSD), providing high selectivity.

The stability tests of prepared h-FABP immunosensor were performed at 4.0 °C for 6 weeks in the presence of 1.0 mM

Table 1 The comparison of electrochemical h-FABP immunosensor with other reported techniques

Material/method	Linear range	LOD	Ref.
2D Ni-MOF	100.0 fg mL^{-1}–1000.0 ng mL^{-1}	44.5 fg mL^{-1}	[22]
Immunoturbidimetric assay	2.76–115.0 ng mL^{-1}	2.40 ng mL^{-1}	[71]
Impedimetric immunoassay	98.0 pg mL^{-1}–100.0 ng mL^{-1}	117.0 pg mL^{-1}	[20]
Capacitive immunosensor	98.0 pg mL^{-1}–100.0 ng mL^{-1}	0.84 ng mL^{-1}	[21]
CL immunoassay	1.0 pg mL^{-1}–1.0 ng mL^{-1}	0.32 pg mL^{-1}	[72]
Thermal sensing	1.50–75.0 ng mL^{-1}	1.50 ng mL^{-1}	[73]
Multiplexed chemiluminescence	0.10 pg mL^{-1}–.0 µg mL^{-1}	0.06 pg mL^{-1}	[74]
Electrochemical immunosensor	0.01–1.00 pg mL^{-1}	3.30 fg mL^{-1}	This study

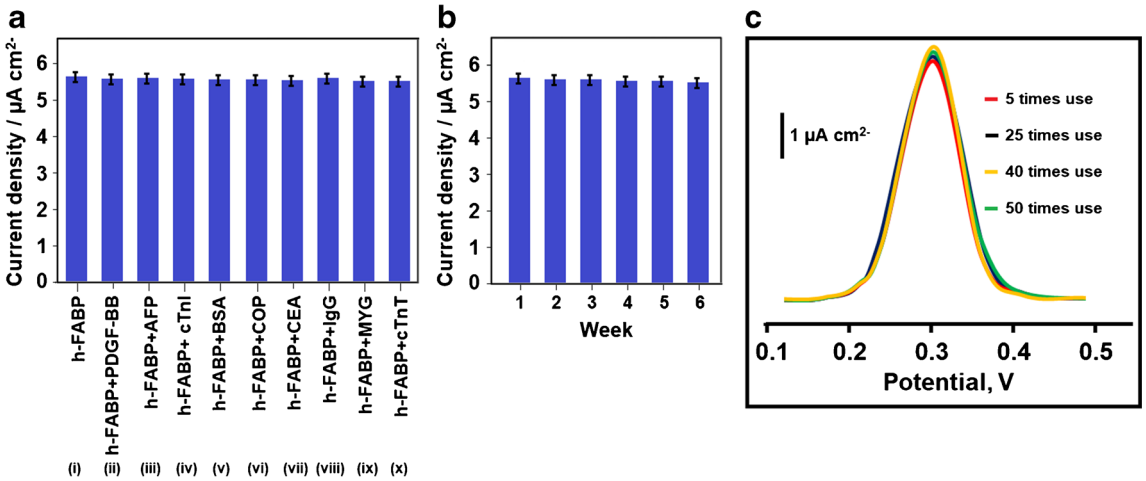

Fig. 8 **a** Immunosensor selective responses against the prepared solutions ($n = 6$): (i) 0.100 pg mL^{-1} h-FABP, (ii) 0.100 pg mL^{-1} h-FABP +10.00 pg mL^{-1} PDGF-BB, (iii) 0.100 pg mL^{-1} h-FABP +10.00 pg mL^{-1} AFP, (iv) 0.100 pg mL^{-1} h-FABP +10.00 pg mL^{-1} cTnI, (v) 0.100 pg mL^{-1} h-FABP+10.00 pg mL^{-1} BSA, (vi) 0.100 pg mL^{-1} h-FABP+10.00 pg mL^{-1} COP, (vii) 0.100 pg mL^{-1} h-FABP+10.00 pg mL^{-1} CEA, (viii) 0.100 pg mL^{-1} h-FABP+ 10.00 pg mL^{-1} IgG, (ix) 0.100 pg mL^{-1} h-FABP+10.00 pg mL^{-1} MYG and (x) 0.100 pg mL^{-1} h-FABP+10.00 pg mL^{-1} cTnT. **b** Stability test of electrochemical h-FABP immunosensors including 0.100 pg mL^{-1} h-FABP protein ($n = 6$) at 4.0 °C. **c** Reusability test of one electrochemical h-FABP immunosensor including 0.100 pg mL^{-1} h-FABP protein

H_2O_2. According to Fig. 8b, the minimal changes with 0.97% RSD verified the perfect stability of the prepared h-FABP immunosensor (Fig. 8b). Twenty-five different h-FABP immunosensors including 0.100 pg mL^{-1} h-FABP protein were prepared for reproducibility test, and each electrochemical h-FABP immunosensor was used in the presence of 1.0 mM H_2O_2 in 0.1 M PBS (pH 7.0). Thereby, 0.19% of RSD suggested the reliability of the immunosensor production procedure.

Finally, the reusability of the prepared h-FABP immunosensor was evaluated in 1.0-mM H_2O_2 solution (Fig. 8c). The obtained continuous current signals on one prepared h-FABP immunosensor showed 0.79% of RSD during 50 times usage for 20 min, suggesting high reusability.

Conclusions

In conclusion, we developed the electrochemical immunosensor for selective detection of h-FABP with the detection limit of 3.30 fg mL^{-1}. This performance is attributed to the following reasons. (i) hc-g-C_3N_4@CDs not only showed high crystallinity structure and larger surface area, but also acted as ideal carrier for the efficient immobilization of h-FABP-Ab_1. (ii) Significant synergistic effect between $Cd_{0.5}Zn_{0.5}S$ and 7wt%d-$Ti_3C_2T_x$MXene could facilitate electron transfer, providing enhanced sensitivity. In addition, under optimal conditions, the prepared electrochemical immunosensor showed satisfactory selectivity, stability, and reusability. To the best of our knowledge, h-FABP protein determination was firstly prepared based on core-shell high-crystalline graphitic carbon nitride@carbon dots and $Cd_{0.5}Zn_{0.5}S$/d-$Ti_3C_2T_x$ MXene composite. Hence, graphitic carbon nitride@carbon dots and $Cd_{0.5}Zn_{0.5}S$/d-$Ti_3C_2T_x$ MXene as promising functional nanocomposites may be utilized for the production of new generation biosensors in the future.

Supplementary Information The online version contains supplementary material available at https://doi.org/10.1007/s00604-021-04838-6.

Acknowledgements Mehmet Lütfi YOLA would like to thank the Turkish Academy of Sciences for their invaluable support in respect to The Young Scientists Award Programme, TÜBA-GEBIP (2019). The study was partially supported by this award.

Declarations

Conflict of interest The authors declare that they have no competing interests.

References

1. Anderson JL, Morrow DA (2017) Acute myocardial infarction. New Engl J Med 376(21):2053–2064
2. ten Berg JM, Deneer VH (2012) Antiplatelet therapy: does CYP2C19 genotype affect clinical outcome? Nat Rev Cardiol 9(4):192–194
3. Ye XD, He Y, Wang S, Wong GT, Irwin MG, Xia Z (2018) Heart-type fatty acid binding protein (H-FABP) as a biomarker for acute myocardial injury and long-term post-ischemic prognosis. Acta Pharmacol Sin 39(7):1155–1163
4. Rezar R, Jirak P, Gschwandtner M, Derler R, Felder TK, Haslinger M, Kopp K, Seelmaier C, Granitz C, Hoppe UC, Lichtenauer M

(2020) Heart-type fatty acid-binding protein (H-FABP) and its role as a biomarker in heart failure: what do we know so far? J Clin Med 9(1):164
5. Ohkaru Y, Asayama K, Ishii H, Nishimura S, Sunahara N, Tanaka T, Kawamura K (1995) Development of a sandwich enzyme-linked immunosorbent assay for the determination of human heart type fatty acid-binding protein in plasma and urine by using two different monoclonal antibodies specific for human heart fatty acid-binding protein. J Immunol Methods 178(1):99–111
6. Savin M, Mihailescu CM, Matei I, Stan D, Moldovan CA, Ion M, Baciu I (2018) A quantum dot-based lateral flow immunoassay for the sensitive detection of human heart fatty acid binding protein (hFABP) in human serum. Talanta. 178:910–915
7. Karimi-Maleh H, Karimi F, Alizadeh M, Sanati AL (2020) Electrochemical sensors, a bright future in the fabrication of portable kits in analytical systems. Chem Rec 20(7):682–692
8. Khodadadi A, Faghih-Mirzaei E, Karimi-Maleh H, Abbaspourrad A, Agarwal S, Gupta VK (2019) A new epirubicin biosensor based on amplifying DNA interactions with polypyrrole and nitrogen-doped reduced graphene: experimental and docking theoretical investigations. Sensor Actuat B-Chem 284:568–574
9. Tahernejad-Javazmi F, Shabani-Nooshabadi M, Karimi-Maleh H (2019) 3D reduced graphene oxide/FeNi3-ionic liquid nanocomposite modified sensor; an electrical synergic effect for development of tert-butylhydroquinone and folic acid sensor. Compos Part B-Eng 172:666–670
10. Ricci F, Volpe G, Micheli L, Palleschi G (2007) A review on novel developments and applications of immunosensors in food analysis. Anal Chim Acta 605(2):111–129
11. Karimi-Maleh H, Arotiba OA (2020) Simultaneous determination of cholesterol, ascorbic acid and uric acid as three essential biological compounds at a carbon paste electrode modified with copper oxide decorated reduced graphene oxide nanocomposite and ionic liquid. J Colloid Interface Sci 560:208–212
12. Tahernejad-Javazmi F, Shabani-Nooshabadi M, Karimi-Maleh H (2018) Analysis of glutathione in the presence of acetaminophen and tyrosine via an amplified electrode with MgO/SWCNTs as a sensor in the hemolyzed erythrocyte. Talanta. 176:208–213
13. Karimi-Maleh H, Yola ML, Atar N, Orooji Y, Karimi F, Kumar PS, Rouhi J, Baghayeri M (2021) A novel detection method for organophosphorus insecticide fenamiphos: molecularly imprinted electrochemical sensor based on core-shell Co3O4@MOF-74 nanocomposite. J Colloid Interface Sci 592:174–185
14. Asif M, Liu HW, Aziz A, Wang HT, Wang ZY, Ajmal M, Xiao F, Liu HF (2017) Core-shell iron oxide-layered double hydroxide: high electrochemical sensing performance of H2O2 biomarker in live cancer cells with plasma therapeutics. Biosens Bioelectron 97: 352–359
15. Ashraf G, Asif M, Aziz A, Iftikhar T, Liu HF (2021) Rice-spikelet-like copper oxide decorated with platinum stranded in the CNT network for electrochemical in vitro detection of serotonin. ACS Appl Mater Interfaces 13(5):6023–6033
16. Asif M, Aziz A, Azeem M, Wang ZY, Ashraf G, Xiao F, Chen XD, Liu HF (2018) A review on electrochemical biosensing platform based on layered double hydroxides for small molecule biomarkers determination. Adv Colloid Interfac 262:21–38
17. Asif M, Wang HT, Shuang D, Aziz A, Zhang GA, Xiao F, Liu HF (2017) Metal oxide intercalated layered double hydroxide nanosphere: with enhanced electrocatalyic activity towards H2O2 for biological applications. Sensor Actuat B-Chem 239:243–252
18. Asif M, Aziz A, Wang ZY, Ashraf G, Wang JL, Luo HB, Chen XD, Xiao F, Liu HF (2019) Hierarchical CNTs@CuMn layered double hydroxide nanohybrid with enhanced electrochemical performance in H2S detection from live cells. Anal Chem 91(6):3912–3920
19. O'Regan TM, Pravda M, O'Sullivan CK, Guilbault GG (2002) Development of a disposable immunosensor for the detection of human heart fatty-acid binding protein in human whole blood using screen-printed carbon electrodes. Talanta. 57(3):501–510
20. Stan D, Mihailescu CM, Iosub R, Moldovan C, Savin M, Baciu I (2012) Electrochemical studies of homogeneous self-assembled monolayers versus mixed self-assembled monolayers on gold electrode for "label free" detection of heart fatty acid binding protein. Thin Solid Films 526:143–149
21. Mihailescu CM, Stan D, Iosub R, Moldovan C, Savin M (2015) A Sensitive capacitive immunosensor for direct detection of human heart fatty acid-binding protein (h-FABP). Talanta. 132:37–43
22. Gan XF, Han DB, Wang JM, Liu P, Li XR, Zheng QY, Yan YR (2021) A highly sensitive electrochemiluminescence immunosensor for h-FABP determination based on self-enhanced luminophore coupled with ultrathin 2D nickel metal-organic framework nanosheets. Biosens Bioelectron 171:112735
23. Hao XQ, Zhou J, Cui ZW, Wang YC, Wang Y, Zou ZG (2018) Zn-vacancy mediated electron-hole separation in ZnS/g-C3N4 heterojunction for efficient visible-light photocatalytic hydrogen production. Appl Catal B-Environ 229:41–51
24. Sun T, Jiang HY, Ma CC, Mao F, Xue B (2016) Ag/g-C3N4 photocatalysts: microwave-assisted synthesis and enhanced visible-light photocatalytic activity. Catal Commun 79:45–48
25. Sun HR, Guo F, Pan JJ, Huang W, Wang K, Shi WL (2021) One-pot thermal polymerization route to prepare N-deficient modified g-C3N4 for the degradation of tetracycline by the synergistic effect of photocatalysis and persulfate-based advanced oxidation process. Chem Eng J 406:126844
26. Shi WL, Liu C, Li MY, Lin X, Guo F, Shi JY (2020) Fabrication of ternary Ag3PO4/Co-3(PO4)(2)/g-C3N4 heterostructure with following type II and Z-scheme dual pathways for enhanced visible-light photocatalytic activity. J Hazard Mater 389:121907
27. Kumar A, Kumari A, Sharma G, Du B, Naushad M, Stadler FJ (2020) Carbon quantum dots and reduced graphene oxide modified self-assembled S@C3N4/B@C3N4 metal-free nano-photocatalyst for high performance degradation of chloramphenicol. J Mol Liq 300:112356
28. Ong WJ, Tan LL, Ng YH, Yong ST, Chai SP (2016) Graphitic carbon nitride (g-C3N4)-based photocatalysts for artificial photosynthesis and environmental remediation: are we a step closer to achieving sustainability? Chem Rev 116(12):7159–7329
29. Tay Q, Kanhere P, Ng CF, Chen S, Chakraborty S, Huan ACH, Sum TC, Ahuja R, Chen Z (2015) Defect engineered g-C3N4 for efficient visible light photocatalytic hydrogen production. Chem Mater 27(14):4930–4933
30. Li H, Wang HB, Guo JQ, Ye S, Shi WL, Peng X, Song J, Qu JL (2020) Long-wavelength excitation of carbon dots as the probe for real-time imaging of the living-cell cycle process. Sensor Actuat B-Chem 311:127891
31. Liu CY, Huang HW, Cui W, Dong F, Zhang YH (2018) Band structure engineering and efficient charge transport in oxygen substituted g-C3N4 for superior photocatalytic hydrogen evolution. Appl Catal B-Environ 230:115–124
32. Ansari MS, Banik A, Qureshi M (2017) Morphological tuning of photo-booster g-C3N4 with higher surface area and better charge transfers for enhanced power conversion efficiency of quantum dot sensitized solar cells. Carbon. 121:90–105
33. Zeng DQ, Zhou T, Ong WJ, Wu MD, Duan XG, Xu WJ, Chen YZ, Zhu YA, Peng DL (2019) Sub-5 nm ultra-fine FeP nanodots as efficient co-catalysts modified porous g-C3N4 for precious-metal-free photocatalytic hydrogen evolution under visible light. ACS Appl Mater Interfaces 11(6):5651–5660
34. Shi WL, Wang JB, Yang S, Lin X, Guo F, Shi JY (2020) Fabrication of a ternary carbon dots/CoO/g-C3N4 nanocomposite photocatalyst with enhanced visible-light-driven photocatalytic hydrogen production. J Chem Technol Biotechnol 95(8):2129–2138

35. Handoko AD, Steinmann SN, Seh ZW (2019) Theory-guided materials design: two-dimensional MXenes in electro- and photocatalysis. Nanoscale Horiz 4(4):809–827
36. Lim KRG, Handoko AD, Nemani SK, Wyatt B, Jiang HY, Tang JW, Anasori B, Seh ZW (2020) Rational design of two-dimensional transition metal carbide/nitride (MXene) hybrids and nanocomposites for catalytic energy storage and conversion. ACS Nano 14(9): 10834–10864
37. Cai T, Wang LL, Liu YT, Zhang SQ, Dong WY, Chen H, Yi XY, Yuan JL, Xia XN, Liu CB, Luo SL (2018) Ag3PO4/Ti3C2 MXene interface materials as a Schottky catalyst with enhanced photocatalytic activities and anti-photocorrosion performance. Appl Catal B-Environ 239:545–554
38. Handoko AD, Fredrickson KD, Anasori B, Convey KW, Johnson LR, Gogotsi Y, Vojvodic A, Seh ZW (2018) Tuning the basal plane functionalization of two-dimensional metal carbides (MXenes) to control hydrogen evolution activity. Acs Appl Energ Mater 1(1): 173–180
39. Kadirsoy S, Atar N, Yola ML (2020) Molecularly imprinted QCM sensor based on delaminated MXene for chlorpyrifos detection and QCM sensor validation. New J Chem 44(16):6524–6532
40. Ozcan N, Medetalibeyoglu H, Akyildirim O, Atar N, Yola ML (2020) Electrochemical detection of amyloid-beta protein by delaminated titanium carbide MXene/multi-walled carbon nanotubes composite with molecularly imprinted polymer. Mater Today Commun 23:101097
41. Huang F, Hou J, Wang HG, Tang H, Liu ZY, Zhang LS, Zhang QF, Peng SL, Liu JS, Cao GZ (2017) Impacts of surface or interface chemistry of ZnSe passivation layer on the performance of CdS/CdSe quantum dot sensitized solar cells. Nano Energy 32:433–440
42. Kalisman P, Nakibli Y, Amirav L (2016) Perfect photon-to-hydrogen conversion efficiency. Nano Lett 16(3):1776–1781
43. Peng SQ, An R, Li YX, Lu GX, Li SB (2012) Remarkable enhancement of photocatalytic hydrogen evolution over Cd0.5Zn0.5S by bismuth-doping. Int J Hydrog Energ 37(2):1366–1374
44. Yola ML, Atar N, Qureshi MS, Ustundag Z, Solak AO (2012) Electrochemically grafted etodolac film on glassy carbon for Pb(II) determination. Sensor Actuat B-Chem 171:1207–1215
45. Ghidiu M, Lukatskaya MR, Zhao MQ, Gogotsi Y, Barsoum MW (2014) Conductive two-dimensional titanium carbide 'clay' with high volumetric capacitance. Nature. 516(7529):78–U171
46. Yu P, Cao GJ, Yi S, Zhang X, Li C, Sun XZ, Wang K, Ma YW (2018) Binder-free 2D titanium carbide (MXene)/carbon nanotube composites for high-performance lithium-ion capacitors. Nanoscale. 10(13):5906–5913
47. Yola ML (2021) Sensitive sandwich-type voltammetric immunosensor for breast cancer biomarker HER2 detection based on gold nanoparticles decorated Cu-MOF and Cu2ZnSnS4 NPs/Pt/g-C3N4 composite. Microchim Acta 188(3):78
48. Bhunia SK, Jana NR (2014) Reduced graphene oxide-silver nanoparticle composite as visible light photocatalyst for degradation of colorless endocrine disruptors. ACS Appl Mater Interfaces 6(22): 20085–20092
49. Medetalibeyoglu H, Beytur M, Akyildirim O, Atar N, Yola ML (2020) Validated electrochemical immunosensor for ultra - sensitive procalcitonin detection: carbon electrode modified with gold nanoparticles functionalized sulfur doped MXene as sensor platform and carboxylated graphitic carbon nitride as signal amplification. Sensor Actuat B-Chem 319:128195
50. Li ZY, Wang LB, Sun DD, Zhang YD, Liu BZ, Hu QK, Zhou AG (2015) Synthesis and thermal stability of two-dimensional carbide MXene Ti3C2. Mater Sci Eng B-Adv 191:33–40
51. Low JX, Zhang LY, Tong T, Shen BJ, Yu JG (2018) TiO2/MXene Ti3C2 composite with excellent photocatalytic CO2 reduction activity. J Catal 361:255–266
52. Cao SW, Shen BJ, Tong T, Fu JW, Yu JG (2018) 2D/2D Heterojunction of ultrathin MXene/Bi2WO6 nanosheets for improved photocatalytic CO2 reduction. Adv Funct Mater 28(21): 1800136
53. Yu TP, Lv ZH, Wang KH, Sun KL, Liu X, Wang GX, Jiang LH, Xie GW (2019) Constructing SrTiO3-T/CdZnS heterostructure with tunable oxygen vacancies for solar-light-driven photocatalytic hydrogen evolution. J Power Sources 438:227014
54. Jiang JP, Li SB, Hu SJ, Zhang J, Yu WB, Zhou Y (2020) Comparison of high Cr white iron composites reinforced with directly added TiC and in situ formed TiCx. J Mater Res Technol 9(3):3140–3148
55. Meng FT, Umair MM, Iqbal K, Jin X, Zhang SF, Tang BT (2019) Rapid fabrication of noniridescent structural color coatings with high color visibility, good structural stability, and self-healing properties. ACS Appl Mater Interfaces 11(13):13022–13028
56. Wang H, Sun YM, Wu Y, Tu WG, Wu SY, Yuan XZ, Zeng GM, Xu ZCJ, Li SZ, Chew JW (2019) Electrical promotion of spatially photoinduced charge separation via interfacial-built-in quasi-alloying effect in hierarchical Zn2In2S5/Ti3C2(O, OH)x hybrids toward efficient photocatalytic hydrogen evolution and environmental remediation. Appl Catal B-Environ 245:290–301
57. Ning XF, Zhen WL, Wu YQ, Lu GX (2018) Inhibition of CdS photocorrosion by Al2O3 shell for highly stable photocatalytic overall water splitting under visible light irradiation. Appl Catal B-Environ 226:373–383
58. Dai DS, Wang L, Xiao N, Li SS, Xu H, Liu S, Xu BR, Lv D, Gao YQ, Song WY, Ge L, Liu J (2018) In-situ synthesis of Ni2P cocatalyst decorated Zn0.5Cd0.5S nanorods for high quantum-yield photocatalytic hydrogen production under visible light irradiation. Appl Catal B-Environ 233:194–201
59. Yuan YJ, Shen ZK, Wu ST, Su YB, Pei L, Ji ZG, Ding MY, Bai WF, Chen YF, Yu ZT, Zou ZG (2019) Liquid exfoliation of g-C3N4 nanosheets to construct 2D-2D MoS2/g-C3N4 photocatalyst for enhanced photocatalytic H-2 production activity. Appl Catal B-Environ 246:120–128
60. Li YB, Zhang HM, Liu PR, Wang D, Li Y, Zhao HJ (2013) Cross-linked g-C3N4/rGO nanocomposites with tunable band structure and enhanced visible light photocatalytic activity. Small. 9(19): 3336–3344
61. Zhu C, Liu CG, Zhou YJ, Fu YJ, Guo SJ, Li H, Zhao SQ, Huang H, Liu Y, Kang ZH (2017) Carbon dots enhance the stability of CdS for visible-light-driven overall water splitting. Appl Catal B-Environ 216:114–121
62. Zhu C, Liu CA, Fu YJ, Gao J, Huang H, Liu Y, Kang ZH (2019) Construction of CDs/CdS photocatalysts for stable and efficient hydrogen production in water and seawater. Appl Catal B-Environ 242:178–185
63. Hong ZH, Shen BA, Chen YL, Lin BZ, Gao BF (2013) Enhancement of photocatalytic H-2 evolution over nitrogen-deficient graphitic carbon nitride. J Mater Chem A 1(38):11754–11761
64. Chai YY, Liu QQ, Zhang L, Ren J, Dai WL (2017) Structure engineered g-C3N4 nano-sheets by switching the pyrolysis gas atmosphere for enhanced photo-catalytic degradation. Chin J Chem 35(2):173–182
65. Tang H, Chang SF, Jiang LY, Tang GG, Liang W (2016) Novel spindle-shaped nanoporous TiO2 coupled graphitic g-C3N4 nanosheets with enhanced visible-light photocatalytic activity. Ceram Int 42(16):18443–18452
66. Li Y, Feng XH, Lu ZX, Yin H, Liu F, Xiang QJ (2018) Enhanced photocatalytic H-2-production activity of C-dots modified g-C3N4/TiO2 nanosheets composites. J Colloid Interface Sci 513:866–876
67. Yang YM, Liu NY, Qiao S, Liu RH, Huang H, Liu Y (2015) Silver modified carbon quantum dots for solvent-free selective oxidation of cyclohexane. New J Chem 39(4):2815–2821

68. Chang F, Zhang J, Xie YC, Chen J, Li CL, Wang J, Luo JR, Deng BQ, Hu XF (2014) Fabrication, characterization, and photocatalytic performance of exfoliated g-C3N4-TiO2 hybrids. Appl Surf Sci 311:574–581
69. Yao W, Wang XX, Liang Y, Yu SJ, Gu PC, Sun YB, Xu C, Chen J, Hayat T, Alsaedi A, Wang XK (2018) Synthesis of novel flower-like layered double oxides/carbon dots nanocomposites for U (VI) and Am-241(III) efficient removal: Batch and EXAFS studies. Chem Eng J 332:775–786
70. Tambara K, Fujita M, Miyamoto S, Doi K, Nishimura K, Komeda M (2004) Pericardial fluid level of heart-type cytoplasmic fatty acid-binding protein (H-FABP) is an indicator of severe myocardial ischemia. Int J Cardiol 93(2–3):281–284
71. Carless DR, Wnek M, Knox C, Harrison KR, Calder N, Hall AS, Barth JH (2013) Clinical and analytical evaluation of an immunoturbidimetric heart-type fatty acid-binding protein assay. Scand J Clin Lab Invest 73(1):48–53
72. Yang TT, Ren XN, Yang M, Li X, He KK, Rao A, Wan Y, Yang H, Wang SQ, Luo ZQ (2019) A highly sensitive label-free electrochemical immunosensor based on poly (indole-5-carboxylicacid) with ultra-high redox stability. Biosens Bioelectron 141:111406
73. Crapnell RD, Canfarotta F, Czulak J, Johnson R, Betlem K, Mecozzi F, Down MP, Eersels K, van Grinsven B, Cleij TJ, Law R, Banks CE, Peeters M (2019) Thermal detection of cardiac biomarkers heart-fatty acid binding protein and ST2 using a molecularly imprinted nanoparticle-based multiplex sensor platform. Acs Sensors 4(10):2838–2845
74. Li F, Guo L, Hu YT, Li ZM, Liu JC, He JB, Cui H (2020) Multiplexed chemiluminescence determination of three acute myocardial infarction biomarkers based on microfluidic paper-based immunodevice dual amplified by multifunctionalized gold nanoparticles. Talanta. 207:120346